Forward, reverse, and no motion of Marangoni surfers under confinement

Saeed Jafari Kang,[1] Samrat Sur,[2] Jonathan P. Rothstein,[2,*] and Hassan Masoud[1,†]

[1]*Department of Mechanical Engineering–Engineering Mechanics, Michigan Technological University, Houghton, Michigan 49931, USA*

[2]*Department of Mechanical and Industrial Engineering, University of Massachusetts, Amherst, Massachusetts 01003, USA*

(Received 12 March 2020; accepted 16 July 2020; published 12 August 2020)

We examine the mobility of a chemically active particle straddling the interface between a liquid layer of finite depth and a semi-infinite layer of gas. A surface-active agent is released asymmetrically from the particle that locally lowers the interfacial surface tension. It is commonly presumed that the uneven distribution of the surface tension and the associated Marangoni flow lead to the propulsion of the active surfer opposite to the release direction, where the surface tension is higher. This is considered forward motion. However, our recent theoretical analysis—in the limits of negligible inertia and diffusion-dominated transport of the active agent—has shown that this trend may be reversed for certain shapes of the surfer and shallow enough liquid layers. Advancing beyond the Stokes regime, here, we study the Marangoni-driven motion of thin cylindrical disks and oblate spheroids for a wide range of release rates and diffusivity of the exuded chemical species, that control the effective Reynolds and Péclet numbers. We consider various degrees of confinement represented by the thickness of the liquid film, and show that indeed the surfers can undergo a forward, a backward, or an arrested motion. We also identify the links between these modes of mobility and the forces acting on the surfers as well as the flow structure in their vicinity. Rather unexpectedly, we discover that negative pressure is the primary contributor to the fluid force experienced by the surfer and that this suction force is mainly responsible for the reverse Marangoni propulsion. The reported results are based on closely corroborating numerical calculations and experimental measurements.

DOI: 10.1103/PhysRevFluids.5.084004

I. INTRODUCTION

Investigations into the propulsion of floating objects triggered by an automodulation of nearby interfacial stresses date back, at least, to the pioneering work of Lord Rayleigh, in the late 19th century, on the motion of camphor scrapings along a water-air interface [1]. Since then, there have been several other attempts to examine the motion of active particles of various shapes and sizes that self-propel at fluidic interfaces by creating a gradient of surface tension in their immediate vicinity [2–50]. Among the experimental studies, Bassik *et al.* [5] considered the translational and rotational motion of ethanol-soaked poly-N-isopropylacrylamide gels at a water-air interface. Their measurements indicated that the propulsion velocity is linearly related to the spreading speed of ethanol. They also observed that the maximum rotational velocity of the gels is inversely related to their linear dimensions. In a proof-of-concept study, Zhang *et al.* [19] showed the feasibility of using a depolymerization reaction to power the surfing motion of objects ranging from micrometer

*rothstein@ecs.umass.edu
†hmasoud@mtu.edu

to centimeter scales. They observed that microscale particles achieve speeds of up to 660 body lengths per second. Also, Maggi *et al.* [29] designed a continuously rotating microgear that uses the principle of Marangoni propulsion to convert light into mechanical work. In this design, the light absorbed by the gear sitting on a water-air interface locally changes the surface tension, which, in turn, leads to the rotation of the gear. The researchers concluded that the Marangoni propulsion is one of the strongest mechanisms for light actuation at small scales. More recently, Sur *et al.* [49] investigated the dynamics of disk-shaped Marangoni surfers dip coated on one side by a layer of either soap or isopropyl alcohol. Conducting particle tracking and particle image velocimetry (PIV) measurements, they found that the surfers follow a straight steady-state motion at low to moderate speeds, and observed a transition from translational to orbital motion beyond a critical Reynolds number defined based on the propulsion speed of the surfer.

Theoretical efforts to understand the Marangoni propulsion of active surfers include the works of Lauga and Davis [16] and Würger [22], where the propulsion speeds of, respectively, disk-shaped and spherical particles are analytically calculated in the absence of inertia. The derivations involve direct solution of the Stokes equations for the flow of the liquid. The calculations showed that the translational propulsion speed is independent of the size of the particle. In the same context, Masoud and Stone [23] used the reciprocal theorem [51] to bypass detailed calculation of the flow field and derived closed-form expressions for the speed of active oblate and prolate spheroids. There also exist studies on the collective motion of surfers. For instance, Masoud and Shelley [24] considered the dynamics of a flock of chemically active surfers. Their linear stability analysis and numerical simulations using a Fourier pseudospectral method revealed that, if the particles' activity locally raises the surface tension, surface flows of chemical surfers can cause them to clump together—a phenomenon reminiscent of the self-aggregation of slime mold colonies.

Of the cited investigations, the experimental measurements of Soh *et al.* [9] and the mathematical modeling of Vandadi *et al.* [43] uncovered an unexpected phenomenon that a Marangoni surfer may stop propelling or even reverse its motion when placed atop a shallow liquid layer, the thickness of which is comparable to the characteristic length scale of the surfer. This intriguing behavior could be harnessed for sorting interface-trapped active surfers by their size and shape. Realization of such an idea and other potential applications of the reverse Marangoni propulsion, however, requires additional scrutiny of the effect of confinement on the mobility of active surfers. To this end, here, we examine the Marangoni-driven motion of self-propelling disk-shaped and oblate spheroidal particles located at a liquid-gas interface that sits above a liquid layer of finite depth. A combination of numerical simulations and laboratory experiments is employed to systematically study how the particles' aspect ratio and flow parameters such as Reynolds and Péclet numbers influence the speed and direction of the surfers' propulsion at a given thickness of the liquid layer. In particular, force decomposition analysis and flow visualization are used to pinpoint the underlying mechanism for motion reversal. In what follows, we first describe the experimental setup (Sec. II), and then explain the simulation details (Sec. III). The results are discussed next (Sec. IV), and concluding remarks are given in Sec. V.

II. EXPERIMENTAL SETUP AND APPROACH

The experiments involve fabricating a cylindrical disk of radius $R = 2.25$ mm and thickness $\lambda = 1.5$ mm, and a hemisphere of radius $R = 2.375$ mm, both from polydimethlysiloxane, which has a density of $\rho = 965\,\mathrm{Kg/m^3}$. The disk and hemisphere are dip coated into a solution of water and 50% soap (Dawn) to a depth of $d = 1$ mm, as shown in Fig. 1(a). This process results in an asymmetric coating of the particle with a layer of an active agent (i.e., Dawn soap), which is known to reduce the interfacial tension of water from 72 to $\approx 30\,\mathrm{mN/m}$ [52]. The disk or hemisphere is gently placed on the water-air interface and released using tweezers. The dissolution of the coating layer creates a surface tension imbalance that, in turn, leads to the propulsion (also referred to as surfing) of the particle. The experiments are conducted in a clear-walled rectangular container of length $L = 560$ mm and width $W = 45$ mm, that is filled with water [see Fig. 1(a)]. To investigate the

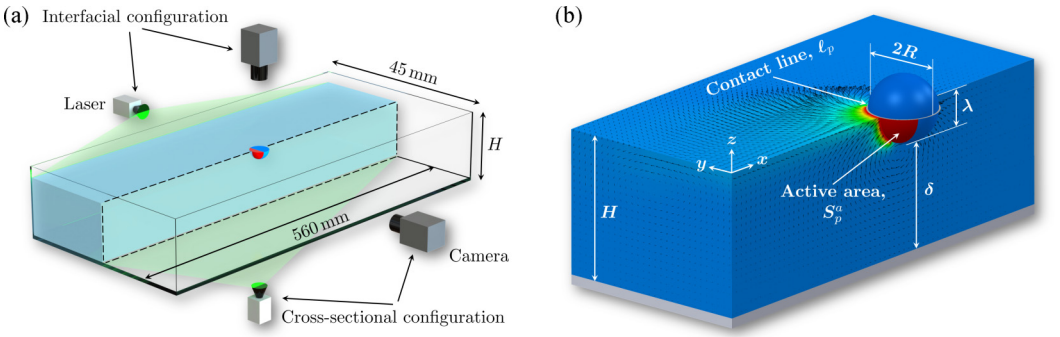

FIG. 1. Schematics of (a) experimental and (b) computational setups depicting, respectively, a fully submerged hemispherical and a half-submerged spherical surfer at a water-air interface. The area of the hemisphere dip coated with a layer of Dawn soap is colored red in panel (a), similar to the active area of the sphere in panel (b). The color map and vector plots in panel (b) represent the concentration distribution and liquid velocity field in the vicinity of the surfer, respectively.

effect of confinement on the motion of the particles, the depth of water is varied from $H = 1.8$ to 10 mm.

We employ particle image velocimetry to analyze the flow field at the water-air interface and beneath the surfer. PIV measurements are performed using uniformly dispersed tracer particles of 40-μm diameter that are illuminated by a 300-mW argon-ion laser light sheet of thickness 1 mm. The laser is oriented either parallel to the interface just below the surface (in order to obtain the interfacial velocity profiles) or normal to the surface passing up through the fluid from the bottom of the container [see Fig. 1(a)]. Through this second configuration, the velocity field underneath the surfer is measured. A high speed camera at a maximum frame rate of 110 fps is utilized to capture the images, which are then processed via a commercial PIV software package developed by LaVision. Also, a digital camera is used to track the motion of the surfer. The videos are captured at 17 fps and fed into a particle tracking software (Tracker) to measure the speed and direction of the particle's propulsion.

III. COMPUTATIONAL SETUP AND NUMERICAL SCHEME

For the purposes of the simulations, we model the motion of a particle located at the interface between a semi-infinite layer of gas and a layer of liquid—with density ρ, viscosity μ, and surface tension γ—that is bounded from below by an impermeable solid wall at a distance H from the interface [see Fig. 1(b)]. Consistent with the experiments, the movement of the particle is caused by an asymmetric release of a chemical species—with diffusivity $\mathcal{D}$—from the "active" region of the particle's surface, which we denote S_p^a [see Fig. 1(b)]. The shape of the particle is considered to be an oblate spheroid of equatorial radius R and aspect ratio (ratio of polar to equatorial radius) ε. We also consider, for the sake of comparison with the experiments, a cylindrical disk of radius R and half-thickness-to-radius ratio of $2/3$.

To reduce the complexity of numerical calculations, the following justifiable assumptions are made.

(i) The liquid-gas interface is flat.

(ii) The particle is half submerged forming a 90° contact angle.

(iii) The released chemical species is soluble into the bulk of the liquid layer and its concentration is constant at S_p^a.

(iv) The liquid is Newtonian with constant density and viscosity that are unaffected by the presence of the solute.

(v) The surface tension of the liquid varies linearly with the concentration of the active agent.

(vi) The particle undergoes a pure translational motion along a straight line parallel to the interface.

Let $\boldsymbol{r} = x\boldsymbol{e}_x + y\boldsymbol{e}_y + z\boldsymbol{e}_z$ be the position vector in the Cartesian coordinate system (x, y, z), with the unit vectors $\boldsymbol{e}_x$, $\boldsymbol{e}_y$, and $\boldsymbol{e}_z$ such that $\boldsymbol{e}_x$ is parallel to the direction of the surfer's propulsion and $\boldsymbol{e}_z$ is normal to the interface pointing away from the liquid [see Fig. 1(b)]. Also, let $\boldsymbol{u}(\boldsymbol{r}, t) = u_x\boldsymbol{e}_x + u_y\boldsymbol{e}_y + u_z\boldsymbol{e}_z$, $p(\boldsymbol{r}, t)$, and $c(\boldsymbol{r}, t)$ represent, respectively, the velocity and pressure fields of the liquid and the concentration distribution of the chemical species, where t denotes the time variable. With these definitions and the above-mentioned conditions, the equations that govern the spatiotemporal evolution of $\boldsymbol{u}$, p, and c are

$$\rho\left(\frac{\partial \boldsymbol{u}}{\partial t} + \boldsymbol{u}\cdot\nabla\boldsymbol{u}\right) = -\nabla p + \mu\nabla^2\boldsymbol{u} \quad \text{and} \quad \nabla\cdot\boldsymbol{u} = 0,$$

$$\text{with} \quad \boldsymbol{u}(\boldsymbol{r}, 0) = \boldsymbol{0}, \quad \boldsymbol{u} = U\boldsymbol{e}_x \quad \text{for} \quad \boldsymbol{r}\in S_p, \quad \boldsymbol{u} = \boldsymbol{0} \quad \text{for} \quad \boldsymbol{r}\in S_w,$$

$$u_z = 0 \quad \text{and} \quad (\boldsymbol{I} - \boldsymbol{nn})\cdot(\boldsymbol{n}\cdot\boldsymbol{\Sigma}) = \mu\left(\frac{\partial u_x}{\partial z}\boldsymbol{e}_x + \frac{\partial u_y}{\partial z}\boldsymbol{e}_y\right)$$

$$= -\nabla_s\gamma = -\left(\frac{\partial \gamma}{\partial x}\boldsymbol{e}_x + \frac{\partial \gamma}{\partial y}\boldsymbol{e}_y\right) \quad \text{for} \quad \boldsymbol{r}\in S_i, \tag{1}$$

$$\frac{\partial c}{\partial t} + \boldsymbol{u}\cdot\nabla\boldsymbol{c} = \mathcal{D}\nabla^2\boldsymbol{c},$$

$$\text{with} \quad c(\boldsymbol{r}, 0) = 0, \quad c = c_s \text{ for } \boldsymbol{r}\in S_p^a, \quad \boldsymbol{n}\cdot\nabla c = 0 \quad \text{for} \quad \boldsymbol{r}\notin S_p^a, \tag{2}$$

where

$$\boldsymbol{\Sigma} = -p\boldsymbol{I} + \mu[\nabla\boldsymbol{u} + (\nabla\boldsymbol{u})^T], \quad \gamma = \gamma_0 - \alpha\, c.$$

Here, S_p, S_w, S_i, $\boldsymbol{\Sigma}$, $\boldsymbol{I}$, and $\boldsymbol{n}$ denote the wetted surface of the surfer, the bounding walls, the liquid-gas interface, the stress tensor, the identity tensor, and the unit normal vector, respectively. Additionally, c_s, γ_0, and α are positive constant parameters. Also, the instantaneous velocity of the surfer U is determined via

$$\int_{\ell_p} \gamma\boldsymbol{t}\, d\ell + \int_{S_p} \boldsymbol{n}\cdot\boldsymbol{\Sigma}\, dS = m\frac{dU}{dt}\boldsymbol{e}_x \quad \text{with} \quad U(0) = 0, \tag{3}$$

where the sum of the integrals represents the total force experienced by the surface (ignoring the drag exerted by the gas phase), ℓ_p denotes the three-phase contact line, $\boldsymbol{t}$ is the unit vector tangent to S_i and normal to ℓ_p, and m is the mass of the surfer.

To avoid dealing with a moving boundary, we rewrite the coupled initial-boundary-value problem described by the Navier-Stokes Eqs. (1), the advection-diffusion Eq. (2), and Newton's equation of motion (3) in a noninertial reference frame attached to the surfer (see, e.g., [53]). The process involves substituting $\boldsymbol{u}$ with $\boldsymbol{v} = \boldsymbol{u} - U\boldsymbol{e}_x$ in Eqs. (1) and (2) and adding a source term equal to $-\rho\, dU/dt\, \boldsymbol{e}_x$ to the right-hand side of the momentum balance expression in Eq. (1). The transformed system of equations is then solved via a second-order finite-volume method as implemented in OPENFOAM (see, e.g., [54]). In particular, the PIMPLE algorithm is employed to treat the pressure-velocity coupling, the Laplacians are discretized via the second-order linear Gaussian integration, the corrected scheme (with the number of corrections set to 2) is used to calculate surface normal gradients, the time derivatives are approximated by the second-order backward differentiation formula, and the equation of motion for the surfer is integrated using the Newmark method with the relaxation parameter set to 0.5.

Our computational domain is a rectangular box (of length L, width W, and height H) with the submerged volume of the surfer carved out of its top center [see Fig. 1(b)]. This domain is discretized using the SNAPPYHEXMESH utility in a multiblock fashion, where the mesh is densely distributed near the surfer. Grid-independence tests are performed by refining the mesh and

repeating the simulations. In all cases considered, the computational grid is chosen such that the change in the results due to the refinement is marginal. When the simulations are intended for comparison with the experiments, the size of the domain and the depth of the particle's active region are matched with those reported in Sec. II. Otherwise, we set $L = 100R$, $W = 50R$, and $d = R/2$, and vary H to adjust the degree of confinement. Finally, the outlined numerical approach is validated against the analytical calculations of Vandadi *et al.* [43].

IV. RESULTS AND DISCUSSION

To analyze the propulsion behavior of a surfer, we measure its steady-state velocity $\mathcal{U} = \lim_{t\to\infty} U$ under various levels of confinement, characterized by the depth of the liquid layer H. Next, we normalize $\mathcal{U}$ by its corresponding value for deep layers (i.e., $H \to \infty$), denoted as $\mathcal{U}_\infty$, and plot the results vs

$$\delta/R = (H - \lambda)/R.$$

Here, δ and λ are the minimum gap between the surfer and the confining wall, and the thickness of the submerged volume of the surfer, respectively. In view of the simplifying assumptions enumerated in Sec. III, the quantity $\mathcal{U}/\mathcal{U}_\infty$ is a function of the shape of the surfer and δ/R, as well as the Reynolds and Péclet numbers. These two parameters are defined, respectively, as

$$\mathrm{Re} = 2\rho\,\mathcal{U}_\infty R/\mu \quad \text{and} \quad \mathrm{Pe} = 2\,\mathcal{U}_\infty R/\mathcal{D},$$

and they indicate the relative strength of inertial to viscous effects in the fluid flow, and advection to diffusion effects in the transport of the active agent. It is physically more representative to express Re and Pe in terms of $\mathcal{U}_\infty$ instead of $\mathcal{U}$ because the former more accurately reflects the magnitude of the liquid velocity around the surfer. In the following, we first present the results of experiments and discuss how they compare with the predictions of the computational model. We then report on a more extensive set of numerical data and further elaborate on flow structure variations around the surfer for different sets of parameters.

A. Experimental measurements and comparison with simulations

Figure 2 shows the variation of the normalized propulsion velocity $\mathcal{U}/\mathcal{U}_\infty$ as a function of the dimensionless minimum gap between the surfer and the confining wall δ/R, where the experimental and numerical data points are distinguished by the filled and empty symbols, respectively. The Reynolds numbers corresponding to the motion of the sphere or hemisphere (square symbols) and disk (diamond symbols) are $\mathrm{Re} \approx 23$ and 25, respectively. The Péclet numbers, on the other hand, are of the order of $\mathrm{Pe} \sim \mathcal{O}(10^5)$ in the experiments and are set to $\mathrm{Pe} \approx 1000$ in the simulations, which is believed to be high enough to justify the comparison.

We see that, in all cases, once the gap is greater than several particle radii, the propulsion velocity asymptotes to $\mathcal{U}_\infty$ and is no longer affected by the bounding wall underneath the water-air interface. As the gap decreases and begins to approach the radius of the surfer (i.e., $\delta/R \approx 1$), the confinement effect kicks in, which notably slows down the speed of the surfer. On further narrowing the gap, for experimentally tested surfers (see filled symbols), this trend continues until the surfer comes to rest—even though the fluid around it continues to flow. Beyond this critical point, the surfer reverses its course. The magnitude of the reverse velocity and the crossover depth are functions of, among other factors, the geometry of the surfer and, therefore, differ for the hemisphere and disk. Specifically, a comparison between the plots for the sphere and disk (filled squares and diamonds in Fig. 2) reveals that the gap corresponding to the onset of backward propulsion is several times thinner for the sphere. Furthermore, the maximum rearward speed of the sphere is about an order of magnitude slower than that of the disk, which is about 10% of its $\mathcal{U}_\infty$.

The above experimental observations are largely corroborated by the numerical calculations (see empty symbols), with the exception that, in the simulations, the velocity of the spherical surfer

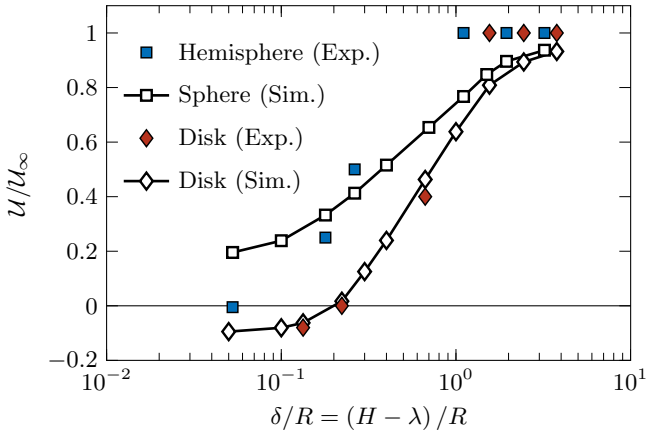

FIG. 2. Comparison between the results of experimental measurements (filled symbols) and numerical calculations (empty symbols) for the normalized propulsion velocity $\mathcal{U}/\mathcal{U}_\infty$ vs the dimensionless minimum gap between the surfer and the confining wall δ/R. The Reynolds numbers corresponding to the motion of the sphere or hemisphere (square symbols) and disk (diamond symbols) are Re ≈ 23 and 25, respectively. The Péclet number is of the order of Pe $\sim \mathcal{O}(10^5)$ in the experiments and is set to Pe ≈ 1000 in the simulations, which is sufficiently high to justify the comparison.

approaches a finite positive value at very small gaps (i.e., $\delta/R \ll 1$). This discrepancy can be attributed to the decay in the release rate of the soap coating with time (which can lead to uncertainty in determining the precise experimental Reynolds number), the local increase in the water viscosity due to the release of the soap from the surface of the sphere, and also the pitching motion of the hemisphere (due to the net torque exerted on its wetted surface) in the experiments. In the next subsection, we will show that the reverse motion for spherical surfers occurs at Reynolds numbers Re $\lessapprox 10$ in our idealized model.

Figures 3 and 4 illustrate the flow structure near the Marangoni surfer for representative data points in Fig. 2. We see that the results of PIV experiments (left columns) agree favorably with those of numerical simulations (right columns), and they both depict the following physical picture. The discharge of the surface tension-reducing agent leads to the propulsion of the surfer and also causes the interface to dilate somewhat radially from a stagnation point adjacent to the release site. This point coincides with the location of minimum interfacial tension (see the last two rows of Figs. 3 and 4). The motion of the surfer combined with the diverging interfacial flow due to the dilation gives rise to a flow pattern underneath the free surface that resembles a deformed vortex ring, particularly when the confinement effect is weak. The vortex originates from the reversed flow in the bulk that is necessary to maintain the conservation of mass (i.e., a divergence-free flow). When projected onto the x-z plane bisecting the surfer, the three-dimensional swirling flow appears as a pair of counter-rotating vortices, one below the surfer and the other one to the left of the stagnation point (see the first rows of Figs. 3 and 4). As the thickness of the liquid layer decreases, the counterclockwise rotating vortex in the wake of the surfer becomes more shallow, with its center moving towards the interface and closer to the stagnation point. Additionally, the clockwise rotating vortex gets compressed and weakened until it disappears upon further reducing the depth of water (see the fourth rows of Figs. 3 and 4). In this situation, a narrow clockwise rotating vortex emerges next to the surfer, opposite to its active side (see the third and fourth rows of Fig. 3 and the fourth row of Fig. 4). This flow feature is more distinct for the case of the disk. Next, we present additional simulation results covering a wider range of parameters than those reported above.

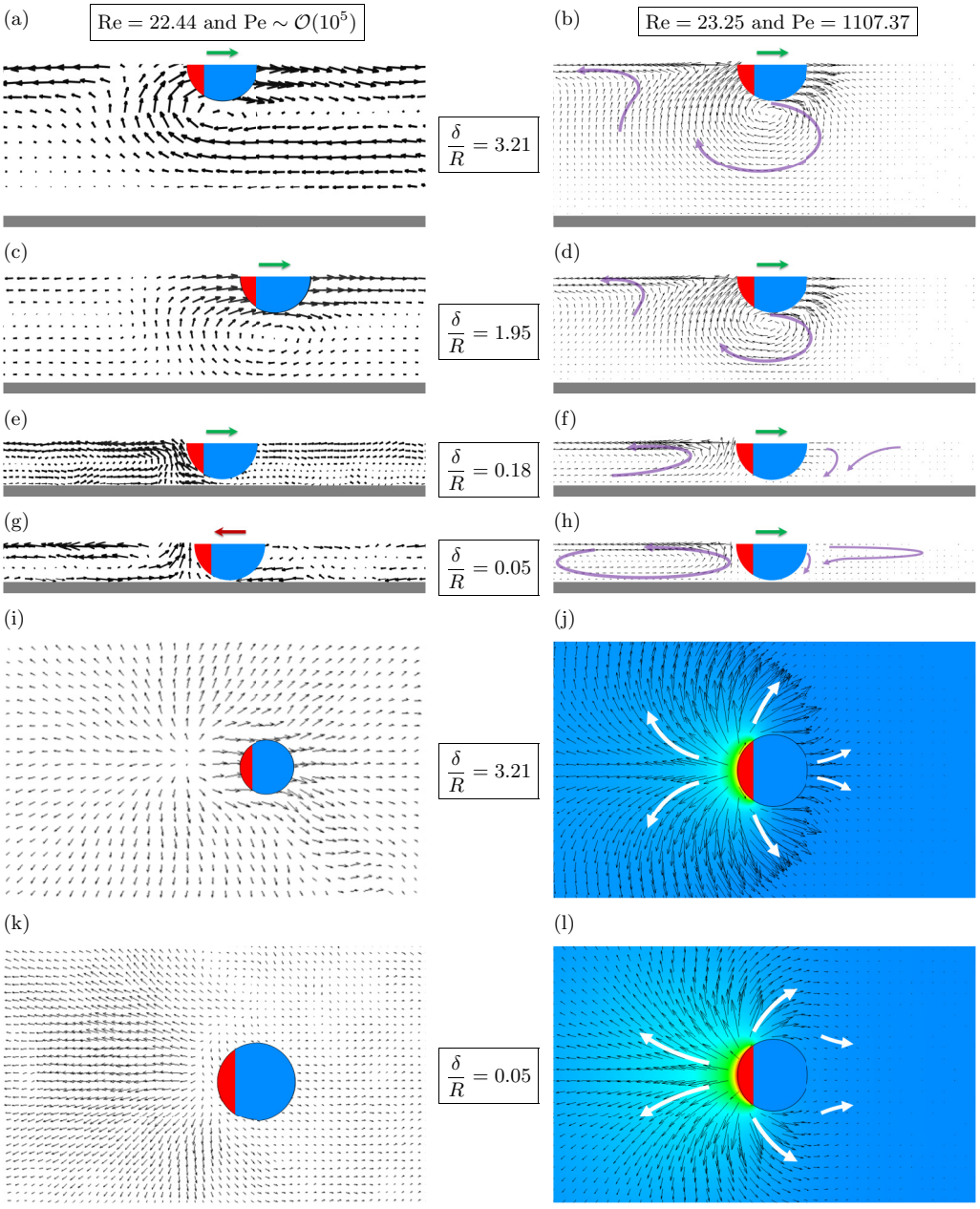

FIG. 3. Flow field plots corresponding to the Marangoni propulsion of a hemisphere or sphere under various degrees of confinement. The results are produced from the PIV measurements (left panels) and numerical simulations (right panels), and are plotted with respect to a fixed frame of reference. The top four rows show the fluid flow in the x-z plane bisecting the surfer, and the fifth and sixth rows illustrate the velocity field at the water-air interface for, respectively, the least and most confined cases (i.e., the first and fourth rows). In the right panels, the thick arrows highlight the direction of the flow and the color maps display the concentration distribution of the active agent, where the concentration is the highest at the active area of the surfer (colored red) and is the lowest at the far field (colored blue). The black arrows are scaled independently in each panel to facilitate flow visualization. The red and green arrows atop each panel show the direction of propulsion and the black circles in the last two rows represent the three-phase contact line.

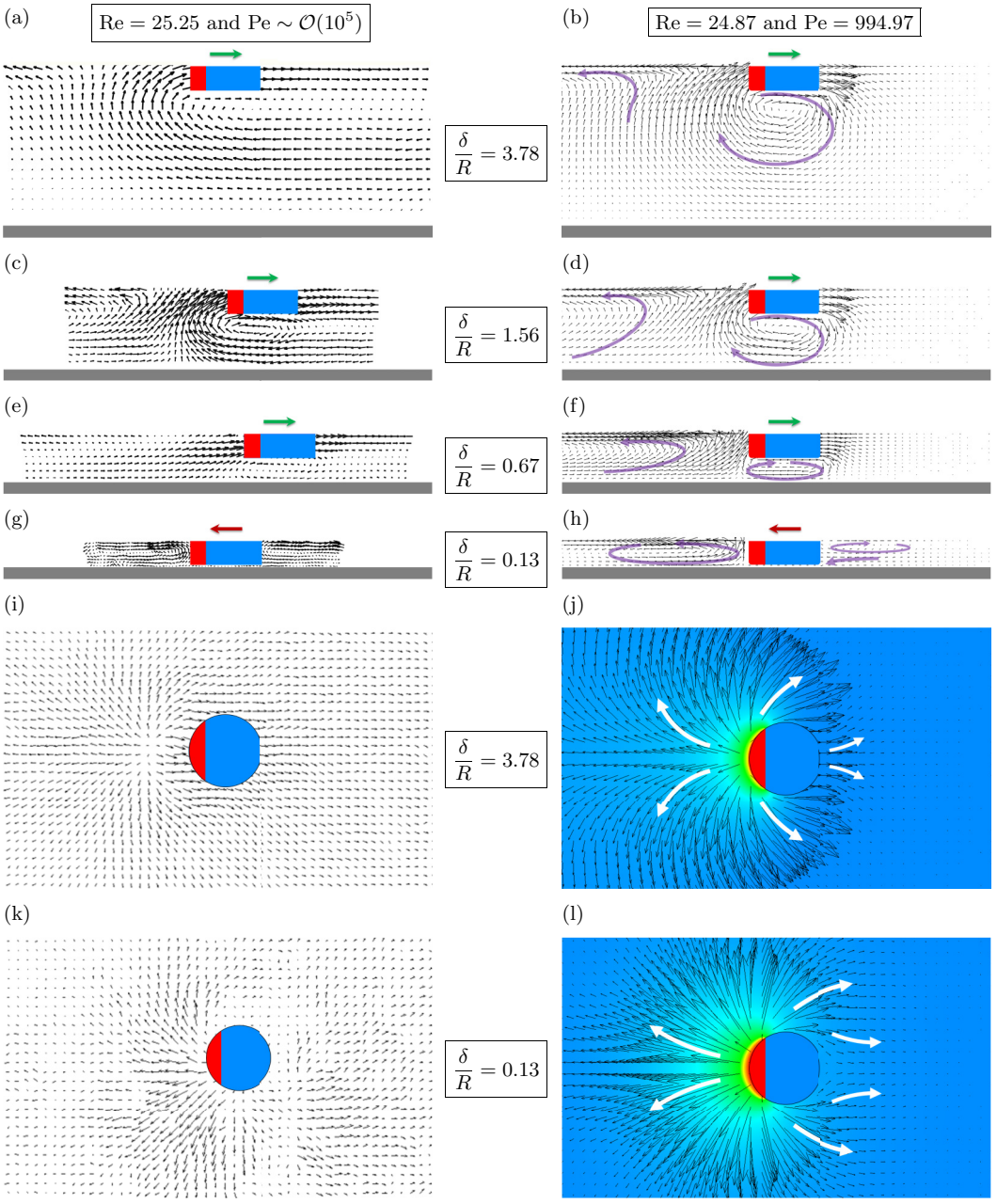

FIG. 4. Flow field plots corresponding to the Marangoni propulsion of a disk under various degrees of confinement. The results are produced from the PIV measurements (left panels) and numerical simulations (right panels), and are plotted with respect to a fixed frame of reference. The top four rows show the fluid flow in the *x*-*z* plane bisecting the surfer, and the fifth and sixth rows illustrate the velocity field at the water-air interface for, respectively, the least and most confined cases (i.e., the first and fourth rows). In the right panels, the thick arrows highlight the direction of the flow and the color maps display the concentration distribution of the active agent, where the concentration is the highest at the active area of the surfer (colored red) and is the lowest at the far field (colored blue). The black arrows are scaled independently in each panel to facilitate flow visualization. The red and green arrows atop each panel show the direction of propulsion and the black circles in the last two rows represent the three-phase contact line.

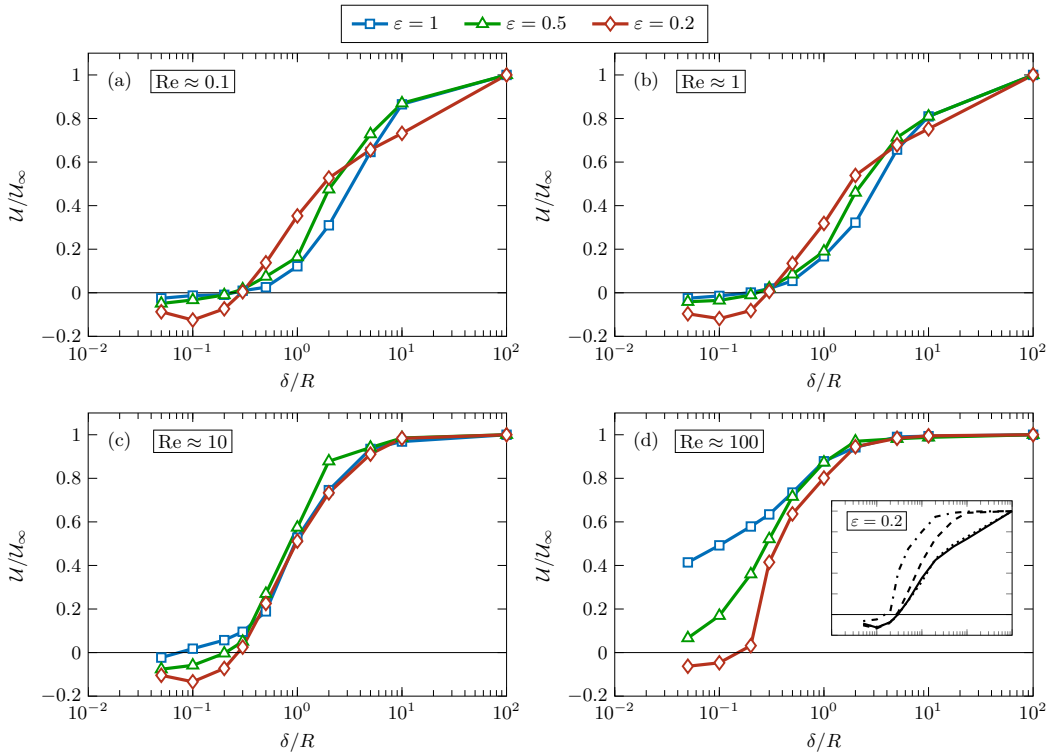

FIG. 5. Normalized propulsion velocity $\mathcal{U}/\mathcal{U}_\infty$ vs the dimensionless minimum gap between the surfer and the confining wall δ/R. The results are shown for Pe $\approx$ 1000 and half-submerged oblate spheroidal surfers of aspect ratio $\varepsilon = 1$, 0.5, and 0.2. Panels (a)–(d) correspond to Re $\approx$ 0.1, 1, 10, and 100, respectively. The inset in panel (d) shows the replots of $\mathcal{U}/\mathcal{U}_\infty$ vs δ/R curves for $\varepsilon = 0.2$ from panels (a)–(d).

B. Additional numerical calculations

Having established the credibility of our computational approach, we now use numerical modeling to examine the effects of Reynolds and Péclet numbers as well as the particle geometry on Marangoni propulsion under confinement. To this end, we simulate the surfing motion of oblate spheroids with aspect ratios $\varepsilon = 1$, 0.5, and 0.2 at Re $\approx$ 0.1, 1, 10, and 100 and Pe $\approx$ 0.1, 10, and 1000. In these simulations, we set $d = R/2$, and increase the length and width of the domain to $L = 100R$ and $W = 50R$ to further lessen the influence of the side boundaries. To avoid flooding the paper with similar-looking figures and redundant descriptions, we only discuss the results for Pe $\approx$ 1000 here and present the plots excluded from the main text in the Supplemental Material [55].

The plots of $\mathcal{U}/\mathcal{U}_\infty$ vs δ/R for each Reynolds number are displayed in Fig. 5. The results for Re $\approx$ 0.1 and 1 are quite alike and they both indicate that all surfers experience the reverse Marangoni propulsion when the liquid layer is sufficiently confined. Specifically, the crossover gap is $\delta/R \approx 0.25$ for $\varepsilon = 1$ (spherical surfer) and $\varepsilon = 0.5$ whereas it is closer to $\delta/R \approx 0.3$ for $\varepsilon = 0.2$ [see Figs. 5(a) and 5(b)]. Also, in all cases, the reverse speed is about or less than 15% of its respective $\mathcal{U}_\infty$. At the moderate Reynolds number of Re $\approx$ 10, we still observe analogous trends, with thicker surfers transitioning from forward to backward motion at narrower gaps [see Fig. 5(c)]. This observation corroborates well with the experimental measurements presented in Fig. 2. When Re is raised by another order of magnitude, however, major changes occur in the propulsion behavior of surfers with moderate to high aspect ratios [see Fig. 5(d)]. In particular, for the cases with $\varepsilon = 1$

TABLE I. Decomposition of the fluid force acting on the surfer for illustrative data points in Figs. 5(c) and 5(d). The subscripts p and v denote the contributions of pressure and viscous forces, respectively. The surfer is assumed to consist of two equal halves, active (which encompasses the release site) and inactive. Additionally, the forces exerted on these regions are distinguished by the superscripts a and ia, respectively. All forces are normalized by the surface tension force $F_{st} = \boldsymbol{e}_x \cdot \int_{\ell_p} \gamma \boldsymbol{t}\, d\ell$, which is equal to the negative of $F = \boldsymbol{e}_x \cdot \int_{S_p} \boldsymbol{n} \cdot \boldsymbol{\Sigma}\, dS = F_p + F_v = F^a + F^{ia}$ with $F_p = F_p^a + F_p^{ia}$, $F_v = F_v^a + F_v^{ia}$, $F^a = F_p^a + F_v^a$, and $F^{ia} = F_p^{ia} + F_v^{ia}$.

ε	$\frac{\delta}{R}$	$\frac{\mathcal{U}}{\mathcal{U}_\infty}$	$\frac{F^a}{F_{st}}$	$\frac{F^{ia}}{F_{st}}$	$\frac{F_p}{F_{st}}$	$\frac{F_v}{F_{st}}$	$\frac{F_p^a}{F_{st}}$	$\frac{F_p^{ia}}{F_{st}}$	$\frac{F_v^a}{F_{st}}$	$\frac{F_v^{ia}}{F_{st}}$
					Re ≈ 10					
1	5	0.93	−0.85	−0.15	−0.74	−0.26	−0.70	−0.04	−0.15	−0.11
1	0.5	0.19	−0.95	−0.05	−0.79	−0.21	−0.80	0.01	−0.15	−0.06
1	0.05	−0.02	−1.12	0.12	−0.89	−0.11	−1.03	0.14	−0.09	−0.02
0.5	5	0.94	−0.81	−0.19	−0.61	−0.39	−0.57	−0.04	−0.24	−0.15
0.5	0.5	0.27	−0.90	−0.10	−0.69	−0.31	−0.68	−0.01	−0.22	−0.09
0.5	0.05	−0.08	−0.21	0.21	−0.86	−0.14	−1.10	0.24	−0.11	−0.03
0.2	5	0.91	−0.77	−0.23	−0.40	−0.60	−0.38	−0.02	−0.39	−0.21
0.2	0.5	0.23	−0.86	−0.14	−0.48	−0.52	−0.48	0.00	−0.38	−0.14
0.2	0.05	−0.10	−1.16	0.16	−0.84	−0.16	−0.94	0.10	−0.22	0.06
					Re ≈ 100					
1	5	0.99	−0.76	−0.24	−0.70	−0.30	−0.66	−0.04	−0.10	−0.20
1	0.5	0.73	−0.83	−0.17	−0.73	−0.27	−0.73	0.00	−0.10	−0.17
1	0.05	0.41	−0.89	−0.11	−0.80	−0.20	−0.81	0.01	−0.08	−0.12
0.5	5	0.98	−0.79	−0.21	−0.59	−0.41	−0.55	−0.04	−0.24	−0.17
0.5	0.5	0.72	−0.83	−0.17	−0.66	−0.34	−0.64	−0.02	−0.19	−0.15
0.5	0.05	0.07	−0.93	−0.07	−0.77	−0.23	−0.78	0.01	−0.15	−0.08
0.2	5	0.98	−0.65	−0.35	−0.39	−0.61	−0.36	−0.03	−0.29	−0.32
0.2	0.5	0.64	−0.74	−0.26	−0.44	−0.56	−0.44	0.00	−0.30	−0.26
0.2	0.05	−0.06	−1.07	0.07	−0.77	−0.23	−0.84	0.07	−0.23	0.00

and 0.5, lowering of the gap no longer alters the propulsion direction. Remarkably, for the spherical surfer, $\mathcal{U}/\mathcal{U}_\infty$ drops to only about 0.4 at the very small gap size of $\delta/R = 0.05$. Overall, we find that, for the range of Re considered, the general behavior of $\mathcal{U}/\mathcal{U}_\infty$ vs δ/R curves is less sensitive to the Reynolds number for low aspect ratio surfers [see the inset in Fig. 5(d) for $\varepsilon = 0.2$]. This could explain why numerical and experimental results matched more closely for the disk in Fig. 2, despite the uncertainty in the actual value of Re in the experiments.

The data in Fig. 5 correspond to the steady-state motion of the surfers. In this condition, the net force acting on the particle in the direction of propulsion is zero, which means that the surface tension force $F_{st} = \boldsymbol{e}_x \cdot \int_{\ell_p} \gamma \boldsymbol{t}\, d\ell$ is balanced by the sum of pressure and viscous forces $F_p + F_v = F = \boldsymbol{e}_x \cdot \int_{S_p} \boldsymbol{n} \cdot \boldsymbol{\Sigma}\, dS$ [see Eq. (3)]. Given the orientation of the (x, y, z) coordinate system with respect to the location of S_p^a, F_{st} is always a positive quantity [see Fig. 1(b)]. Of fundamental interest here are the relative contributions of pressure and viscous forces. It is also of value to have an understanding about the distribution of the forces over S_p. For instance, it is informative to know that if the surfer is divided into two equal halves, say active (which encompasses the release site) and inactive, how F_p, F_v, and their sum F would split between these two regions. Table I provides this information for illustrative points in Fig. 5, where the forces and their subdivisions (denoted by the superscripts a and ia) are normalized by F_{st}.

First, we discover that, in the vast majority of cases considered, much of the resistance to the surface tension force is due to the negative pressure (suction) exerted on the active half of the surfer F_p^a; the far-field pressure is set to zero in the simulations. The rest of the resistance comes from the viscous force F_v (which is more evenly split over S_p than F_p) and the pressure force acting on the inactive side of the surfer F_p^{ia}. The share of the latter is often very small. Consider, for example, the case of $\varepsilon = 0.5$, $\delta/R = 0.5$, and $\mathrm{Re} \approx 10$, for which $F_p/F_{st} = -0.69$ and $F_v/F_{st} = -0.31$, or a more extreme case of $\varepsilon = 1$, $\delta/R = 0.05$, and $\mathrm{Re} \approx 100$, with $F_p/F_{st} = -0.89$ and $F_v/F_{st} = -0.11$. To put these force decompositions into perspective, 2/3 of the Stokes drag on a moving sphere comes from the viscous stresses and the remainder is the contribution of the pressure. Additionally, the pressure drags felt on the front and back sides of the sphere are identical. Our calculations indicate that the relative contribution of F_p^a (and consequently that of F_p) increases with reducing the gap size and decreases mildly with the rise of inertial effects. They also show that F_p/F_{st} is greater for more rounded surfers.

Second, we learn that there exists a link between the direction of surfers' motion and the distribution of the total fluid force on their active and inactive halves. Specifically, we find that the reverse Marangoni propulsion is associated with the fluid force on the active sides of a surfer exceeding that of the surface tension force in the negative direction ($F^a/F_{st} < -1$), which also corresponds to a positive value for the force on the inactive side of the surfer ($0 < F^{ia}/F_{st}$) (see the boxes in Table I). In other words, our force decomposition analysis suggests that once the sum of the suction and viscous forces on the active side of a surfer (which monotonically increases in magnitude with reducing the gap) outweighs the surface tension force then the surfer begins to move in the reverse direction. The change in the direction of motion results in the generation of a positive total force on the other (inactive) side of the surfer to compensate for the excess negative force on its active side, thereby maintaining a steady force balance. As a separate but related matter, we note that, for a given ε and Re, F_{st} is almost invariant to changes in δ/R. The two exceptions are when $\varepsilon = 1$ and 0.5 for $\mathrm{Re} \approx 10$ and $\delta/R = 0.05$. In these cases a decrease of two orders of magnitude in the gap size results in 9 and 13% changes in F_{st}, respectively. By contrast, in other cases the changes are 2% or less.

The results of Fig. 5 and Table I are supplemented by the flow field plots of Figs. 6 and 7, that show the variations of the flow pattern around the surfer with increasing Re at, respectively, low to moderate and extreme confinements. From Fig. 6, we learn that higher Re corresponds to more compact vortices, which is in line with intuition. Consistent with Figs. 3 and 4, we also see that the vortices are compressed as the liquid layer gets shallower. The choice of aspect ratio $\varepsilon = 0.5$ in this figure is immaterial, since the qualitative structure of the flow is insensitive to the thickness of the surfer (see Figs. 3SM–8SM of the Supplemental Material [55]). In contrast, as shown in Fig. 7, when the gap is very thin, the surfer's aspect ratio plays a fundamental role in shaping the flow structure in its vicinity. It also affects how dependent the flow pattern is on Re. For instance, varying Re results in completely distinct flows for $\varepsilon = 1$ and nearly identical ones for $\varepsilon = 0.2$ (see the first and last columns of Fig. 7). We note that, even though not discussed here, the impact of changing the Péclet number on the results presented in this subsection can be deduced from comparison between Fig. 5 and Figs. 1SM and 2SM, and from contrasting Figs. 3SM–8SM with Figs. 9SM–14SM and 15SM–20SM, where, except for Fig. 5, all figures are from the Supplemental Material [55].

Before bringing this section to a close, we would like to briefly comment on how we have modeled the release of the chemical species. In its simplest form, the release process can be simulated by applying either a constant concentration or a constant flux boundary condition on S_p^a. Both of these conditions are capable of faithfully representing the emission of the chemical species, and they produce very similar results provided that their respective release rates match. Here, we have chosen to impose a *depth-invariant* constant concentration at S_p^a because it better mimics the way the soap coating spreads in the experiments and also does not require *a priori* knowledge of the release rate. In our previous study [43] (where the reverse Marangoni propulsion was predicted theoretically in the limits of vanishing Re and Pe), on the other hand, a constant flux boundary condition was applied. There, it was assumed that the release rate of the active agent is

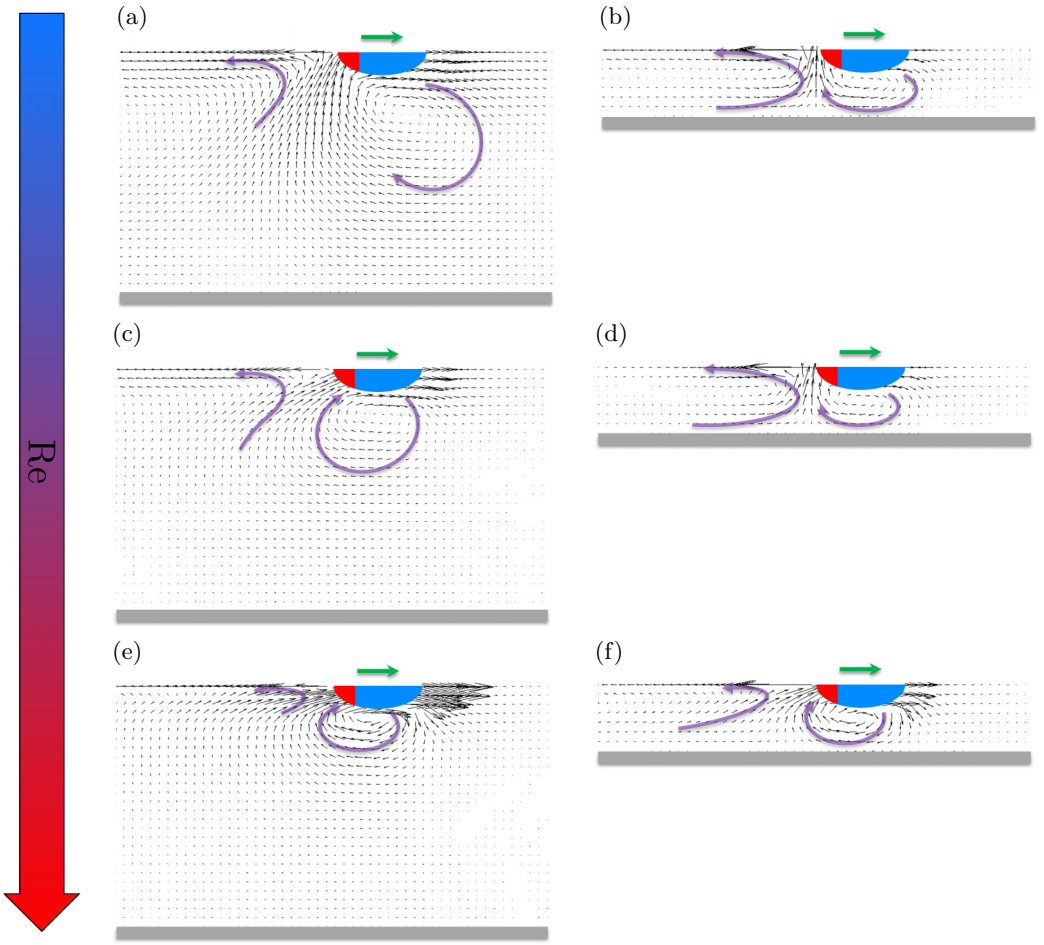

FIG. 6. Flow field plots corresponding to the Marangoni propulsion of a half-submerged oblate spheroid of aspect ratio $\varepsilon = 0.5$. The results are produced from numerical simulations for Pe $\approx$ 1000 (see Fig. 5 and Supplemental Material [55]). The gap size is $\delta/R = 5$ and 1 in the left and right columns, respectively. The Reynolds number increases in each successive row from Re $\approx$ 1 to 10 and then to Re $\approx$ 100. The black arrows are scaled independently in each panel to facilitate flow visualization. The green arrows atop each panel show the direction of propulsion and the purple ones highlight the flow pattern.

fixed and does not change with the gap size. This subtle difference in modeling ought to be taken into account when comparing the results of Figs. 2 and 5 of the main text and Figs. 1SM and 2SM of the Supplemental Material [55] with the analytical calculations of Vandadi *et al.* [43].

V. SUMMARY

We have investigated the propulsion characteristics of Marangoni surfers under confinement. Through experimental measurements and numerical simulations, we demonstrated that, contrary to what might be the usual expectation, the surfers may propel themselves in the direction of lower surface tension. This counterintuitive phenomenon emerges due to the competition between two opposing influences, namely, the net surface tension force acting along the three-phase contact line and the force exerted on the submerged area of the surfer by the flow in the bulk of the liquid

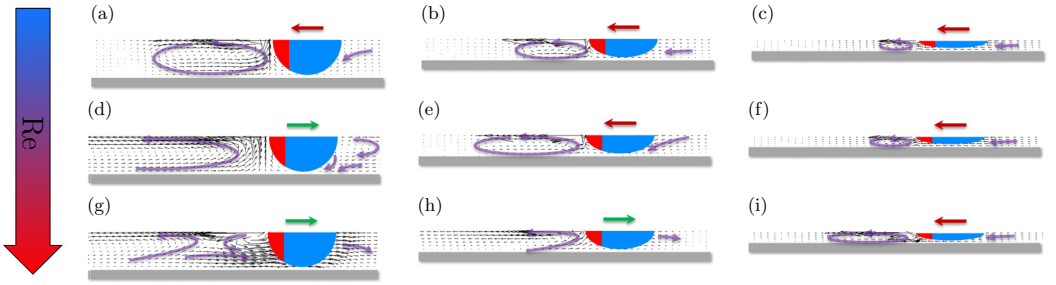

FIG. 7. Flow field plots corresponding to the Marangoni propulsion of half-submerged oblate spheroids of various aspect ratios under extreme confinements ($\delta/R = 0.1$). The results are produced from numerical simulations for Pe $\approx$ 1000 (see Fig. 5 and Supplemental Material [55]). The left, middle, and right columns illustrate the flow for $\varepsilon = 1$, 0.5, and 0.2, respectively. The Reynolds number increases in each successive row from Re $\approx$ 1 to 10 and then to Re $\approx$ 100. The black arrows are scaled independently in each panel to facilitate flow visualization. The red and green arrows atop each panel show the direction of propulsion and the purple ones highlight the flow pattern.

layer, which is induced by the Marangoni stresses at the interface and the motion of the surfer itself. Perhaps surprisingly, we uncovered that a large percentage of the fluid force originates from the negative pressure acting on the active half of the surfer, and that this suction force is the main driving mechanism for the reverse Marangoni propulsion. The fact that viscous stresses are often not the primary contributors to the force balance in Marangoni surfing—even at low Reynolds numbers—appears to be a distinguishing characteristic of this type of motion.

We showed that, at low and intermediate Reynolds numbers (i.e., Re $\lessapprox$ 10), there exists a critical gap size below which the surfers reverse course and move away from the higher surface tension region of their neighborhoods. Our calculations reveal that the existence of the critical gap at higher Reynolds numbers depends on the shape of the surfer, with a greater likelihood for thinner surfers. Furthermore, the simulations indicate that the direction of the Marangoni propulsion is less sensitive to the Péclet number than it is to Re. To provide additional insights into the quantitative results, flow visualizations have been presented throughout the analysis, highlighting the dominant flow features corresponding to various mobility modes of the Marangoni surfers. Overall, our paper has established a basic understanding of Marangoni self-propulsion on liquid layers of finite depth, which is critically needed for broadening the application of this phenomenon in existing and future systems.

In conclusion, it is worth noting that the reverse Marangoni surfing is not necessarily limited to self-propelling surfers. For example, Kavokine *et al.* [56] considered the transport of a liquid marble floating on a water-air interface embedding photosensitive surfactants. They observed that, when the liquid layer beneath the interface is deep, shining UV light at the interface locally increases the surface tension and, therefore, generates a surface flow that carries the marble towards the light source. Interestingly, they showed that the marble is transported in the opposite direction (i.e., away from the source of the UV light) at shallow enough water depths. The authors attributed their observation to the deformation of the interface. However, our findings suggest that, even if the interface deformation is a non-negligible factor, it may not be the sole contributor to the reported phenomenon.

ACKNOWLEDGMENTS

Financial support from the National Science Foundation under Grants No. CBET-1749634 (H.M.) and No. CBET-1705519 (J.P.R.) is acknowledged. This research was carried out in part

using the computational resources provided by the Superior high-performance computing facility at Michigan Technological University.

[1] L. Rayleigh, Measurements of the amount of oil necessary in order to check the motions of camphor upon water, Proc. R. Soc. London **47**, 364 (1889).
[2] S. Nakata, Y. Iguchi, S. Ose, M. Kuboyama, T. Ishii, and K. Yoshikawa, Self-rotation of a camphor scraping on water: New insight into the old problem, Langmuir **13**, 4454 (1997).
[3] H. Kitahata, S.-I. Hiromatsu, Y. Doi, S. Nakata, and M. R. Islam, Self-motion of a camphor disk coupled with convection, Phys. Chem. Chem. Phys. **6**, 2409 (2004).
[4] S. Soh, K. J. Bishop, and B. A. Grzybowski, Dynamic self-assembly in ensembles of camphor boats, J. Phys. Chem. B **112**, 10848 (2008).
[5] N. Bassik, B. T. Abebe, and D. H. Gracias, Solvent driven motion of lithographically fabricated gels, Langmuir **24**, 12158 (2008).
[6] S. Nakata and M. Murakami, Self-motion of a camphor disk on an aqueous phase depending on the alkyl chain length of sulfate surfactants, Langmuir **26**, 2414 (2009).
[7] Y. Shibuya and S. Matsushita, Electric current generation by camphor boats, Mol. Cryst. Liq. Cryst. **504**, 27 (2009).
[8] N. J. Suematsu, S. Nakata, A. Awazu, and H. Nishimori, Collective behavior of inanimate boats, Phys. Rev. E **81**, 056210 (2010).
[9] S. Soh, M. Branicki, and B. A. Grzybowski, Swarming in shallow waters, J. Phys. Chem. Lett. **2**, 770 (2011).
[10] E. Heisler, N. J. Suematsu, A. Awazu, and H. Nishimori, Collective motion and phase transitions of symmetric camphor boats, J. Phys. Soc. Jpn. **81**, 074605 (2012).
[11] C. Luo, H. Li, L. Qiao, and X. Liu, Development of surface tension-driven microboats and microflotillas, Microsyst. Technol. **18**, 1525 (2012).
[12] H. Li, L. Qiao, X. Liu, and C. Luo, Fabrication and testing of a self-propelled, miniaturized PDMS flotilla, Microsyst. Technol. **18**, 1431 (2012).
[13] L. Qiao, D. Xiao, F. K. Lu, and C. Luo, Control of the radial motion of a self-propelled microboat through a side rudder, Sens. Actuat. A **188**, 359 (2012).
[14] R. Sharma, S. T. Chang, and O. D. Velev, Gel-based self-propelling particles get programmed to dance, Langmuir **28**, 10128 (2012).
[15] G. Zhao and M. Pumera, Liquid-liquid interface motion of a capsule motor powered by the interlayer Marangoni effect, J. Phys. Chem. B **116**, 10960 (2012).
[16] E. Lauga and A. M. J. Davis, Viscous Marangoni propulsion, J. Fluid Mech. **705**, 120 (2012).
[17] H. Kitahata, K. Iida, and M. Nagayama, Spontaneous motion of an elliptic camphor particle, Phys. Rev. E **87**, 010901(R) (2013).
[18] T. Bansagi Jr, M. M. Wrobel, S. K. Scott, and A. F. Taylor, Motion and interaction of aspirin crystals at aqueous-air interfaces, J. Phys. Chem. B **117**, 13572 (2013).
[19] H. Zhang, W. Duan, L. Liu, and A. Sen, Depolymerization-powered autonomous motors using biocompatible fuel, J. Am. Chem. Soc. **135**, 15734 (2013).
[20] M. Xiao, C. Jiang, and F. Shi, Design of a uv-responsive microactuator on a smart device for light-induced on-off-on motion, NPG Asia Mater. **6**, e128 (2014).
[21] V. Pimienta and C. Antoine, Self-propulsion on liquid surfaces, Curr. Opin. Colloid Interface Sci. **19**, 290 (2014).
[22] A. Würger, Thermally driven Marangoni surfers, J. Fluid Mech. **752**, 589 (2014).
[23] H. Masoud and H. A. Stone, A reciprocal theorem for Marangoni propulsion, J. Fluid Mech. **741**, R4 (2014).
[24] H. Masoud and M. J. Shelley, Collective Surfing of Chemically Active Particles, Phys. Rev. Lett. **112**, 128304 (2014).

[25] K. Iida, H. Kitahata, and M. Nagayama, Theoretical study on the translation and rotation of an elliptic camphor particle, Physica D **272**, 39 (2014).
[26] K. Nishi, K. Wakai, T. Ueda, M. Yoshii, Y. S. Ikura, H. Nishimori, S. Nakata, and M. Nagayama, Bifurcation phenomena of two self-propelled camphor disks on an annular field depending on system length, Phys. Rev. E **92**, 022910 (2015).
[27] N. J. Suematsu, K. Tateno, S. Nakata, and H. Nishimori, Synchronized intermittent motion induced by the interaction between camphor disks, J. Phys. Soc. Jpn. **84**, 034802 (2015).
[28] C. H. Ooi, A. Van Nguyen, G. M. Evans, O. Gendelman, E. Bormashenko, and N.-T. Nguyen, A floating self-propelling liquid marble containing aqueous ethanol solutions, RSC Adv. **5**, 101006 (2015).
[29] C. Maggi, F. Saglimbeni, M. Dipalo, F. De Angelis, and R. Di Leonardo, Micromotors with asymmetric shape that efficiently convert light into work by thermocapillary effects, Nat. Commun. **6**, 7855 (2015).
[30] J. E. Satterwhite-Warden, D. K. Kondepudi, J. A. Dixon, and J. F. Rusling, Co-operative motion of multiple benzoquinone disks at the air-water interface, Phys. Chem. Chem. Phys. **17**, 29891 (2015).
[31] A. Srinivasan, J. Roche, V. Ravaine, and A. Kuhn, Synthesis of conducting asymmetric hydrogel particles showing autonomous motion, Soft Matter **11**, 3958 (2015).
[32] I. L. Liakos, P. Salvagnini, A. Scarpellini, R. Carzino, C. Beltran, E. Mele, V. Murino, and A. Athanassiou, Biomimetic locomotion on water of a porous natural polymeric composite, Adv. Mater. Interfaces **3**, 1500854 (2016).
[33] S. K. Srivastava and O. G. Schmidt, Autonomously propelled motors for value-added product synthesis and purification, Chem.: Eur. J. **22**, 9072 (2016).
[34] A. Musin, R. Grynyov, M. Frenkel, and E. Bormashenko, Self-propulsion of a metallic superoleophobic micro-boat, J. Colloid Interface Sci. **479**, 182 (2016).
[35] L. Wang, B. Yuan, J. Lu, S. Tan, F. Liu, L. Yu, Z. He, and J. Liu, Self-propelled and long-time transport motion of PVC particles on a water surface, Adv. Mater. **28**, 4065 (2016).
[36] A. Girot, N. Danne, A. Wurger, T. Bickel, F. Ren, J.-C. Loudet, and B. Pouligny, Motion of optically heated spheres at the water-air interface, Langmuir **32**, 2687 (2016).
[37] A. Dominguez, P. Malgaretti, M. N. Popescu, and S. Dietrich, Effective Interaction Between Active Colloids and Fluid Interfaces Induced by Marangoni Flows, Phys. Rev. Lett. **116**, 078301 (2016).
[38] M. Frenkel, G. Whyman, E. Shulzinger, A. Starostin, and E. Bormashenko, Self-propelling rotator driven by soluto-capillary Marangoni flows, Appl. Phys. Lett. **110**, 131604 (2017).
[39] M. Frenkel, V. Multanen, R. Grynyov, A. Musin, Y. Bormashenko, and E. Bormashenko, Camphor-engine-driven micro-boat guides evolution of chemical gardens, Sci. Rep. **7**, 3930 (2017).
[40] W. Fei, Y. Gu, and K. J. Bishop, Active colloidal particles at fluid-fluid interfaces, Curr. Opin. Colloid Interface Sci. **32**, 57 (2017).
[41] H. Nishimori, N. J. Suematsu, and S. Nakata, Collective behavior of camphor floats migrating on the water surface, J. Phys. Soc. Jpn. **86**, 101012 (2017).
[42] Y. Koyano, M. Gryciuk, P. Skrobanska, M. Malecki, Y. Sumino, H. Kitahata, and J. Gorecki, Relationship between the size of a camphor-driven rotor and its angular velocity, Phys. Rev. E **96**, 012609 (2017).
[43] V. Vandadi, S. Jafari Kang, and H. Masoud, Reverse Marangoni surfing, J. Fluid Mech. **811**, 612 (2017).
[44] A. Domínguez and M. N. Popescu, Phase coexistence in a monolayer of active particles induced by Marangoni flows, Soft Matter **14**, 8017 (2018).
[45] M. Frenkel, A. Vilk, I. Legchenkova, S. Shoval, and E. Bormashenko, Mini-generator of electrical power exploiting the Marangoni flow inspired self-propulsion, ACS Omega **4**, 15265 (2019).
[46] H. Morohashi, M. Imai, and T. Toyota, Construction of a chemical motor-movable frame assembly based on camphor grains using water-floating 3D-printed models, Chem. Phys. Lett. **721**, 104 (2019).
[47] H. Gidituri, M. V. Panchagnula, and A. Pototsky, Dynamics of a fully wetted Marangoni surfer at the fluid-fluid interface, Soft Matter **15**, 2284 (2019).
[48] R. J. Löffler, M. M. Hanczyc, and J. Gorecki, A hybrid camphor-camphene wax material for studies on self-propelled motion, Phys. Chem. Chem. Phys. **21**, 24852 (2019).
[49] S. Sur, H. Masoud, and J. P. Rothstein, Translational and rotational motion of disk-shaped Marangoni surfers, Phys. Fluids **31**, 102101 (2019).

[50] K. Dietrich, N. Jaensson, I. Buttinoni, G. Volpe, and L. Isa, Microscale Marangoni surfers, arXiv:2005.06811 (2020).

[51] H. Masoud and H. A. Stone, The reciprocal theorem in fluid dynamics and transport phenomena, J. Fluid Mech. **879**, P1 (2019).

[52] A. Sane, S. Mandre, and I. Kim, Surface tension of flowing soap films, J. Fluid Mech. **841**, R2 (2018).

[53] C. Pozrikidis, *Introduction to Theoretical and Computational Fluid Dynamics* (Oxford University, London, 2011).

[54] F. Moukalled, L. Mangani, and M. Darwish, *The Finite Volume Method in Computational Fluid Dynamics: An Advanced Introduction with OpenFOAM and Matlab*, Fluid Mechanics and Its Applications, Vol. 113 (Springer, New York, 2015).

[55] See Supplemental Material at http://link.aps.org/supplemental/10.1103/PhysRevFluids.5.084004 for velocity field plots related to Figs. 5–7, and for simulation data corresponding to Pe $\approx$ 10 and 0.1.

[56] N. Kavokine, M. Anyfantakis, M. Morel, S. Rudiuk, T. Bickel, and D. Baigl, Light-driven transport of a liquid marble with and against surface flows, Angew. Chem. Int. Ed. **55**, 11183 (2016).